Tailoring the Thermal, Mechanical, and Gas Transport Properties of Cellulose Acetate Membranes with Ionic Liquids for Efficient Propene/Propane Separation

Pegah Hajivand,[a,b] Mariagiulia Longo,[a,*] Teresa Fina Mastropietro,[b] Nicolas Godbert,[b] Marcello Monteleone,[a] C. Grazia Bezzu,[c] Donatella Armentano,[b,*] Johannes C. Jansen[a,*]

[a] Institute on Membrane Technology, CNR-ITM, Via P. Bucci 17/C, 87036, Rende (CS), Italy. E-mail: m.longo@itm.cnr.it, johannescarolus.jansen@cnr.it.

[b] Chemistry and Chemical Technology Department, Università della Calabria, Via P. Bucci 14/C, 87036, Rende (CS), Italy. E-mail: donatella.armentano@unical.it.

[c] Department of Chemistry, Faculty of Science and Engineering, Swansea University, Swansea SA2 8PP, U.K.

ABSTRACT

In light of the importance of designing less energy-intensive and cleaner technologies for olefin purification, the current work aims to systematically enhance the separation of a challenging pair of olefin/paraffin gases, namely propene/propane. To achieve this goal, various blended-membranes are fabricated by mixing cellulose acetate (CA), a carbohydrate-based biopolymer, with three different aprotic ionic liquids (ILs) including $[BMIM]^+[BF_4]^-$, $[BMIM]^+[OTf]^-$, and $[BMIM]^+[Tf_2N]^-$, which are used as additives, with a plasticizer effect, at concentrations in the range of 10-30%. Extensive physicochemical characterization of these membranes by DSC and TGA (thermal properties), Tensile tests (mechanical properties), X-ray diffraction and SEM (structural properties) show that ILs are well-dispersed within the polymeric matrix owing to the interactions between the ILs and CA functional groups. The incorporation of ILs leads to enhanced gas transport properties of the blended membranes compared to the neat one, generally improving their permeability. In particular, the blended-membrane, incorporated with 30% of $[BMIM]^+[Tf_2N]^-$, increased the C_3H_6 permeability by 35 times and the C_3H_6/C_3H_8 selectivity by nearly two times compared to the neat CA membrane. These results suggest that Ionic Liquid-doped cellulose acetate membranes are potential candidates for efficiently separating the propene/propane gas pair.

Keywords

cellulose acetate; ionic liquid; mixed matrix membrane; gas separation; CO_2 capture; propene/propene separation

1. Introduction

The propene/propane mixture is one of the most challenging pairs of gases to separate due to the similar shape, size and physical properties of these gases [1]. Nevertheless, despite the vital role of propene in the industry [2], compared to light gases, relatively few membrane-based works in the literature considered propene/propane separations [3–7]. Cellulose acetate (CA) is one of the first and the most common biopolymers, widely employed for gas separation studies, mostly owing to its non-toxicity and biodegradability, ease of availability [8–10], functional adjustability [11,12], excellent film-forming properties [8], and transportation properties, which are essential for achieving higher gas productivity [13,14]. However, due to its glassy nature, semi-crystalline structure, and trade-off behaviour, there are certain issues associated with CA's application in industrial gas separation processes [15]. In particular, the strong hydrogen bonds in CA structures resulted in a low diffusivity of larger molecules like C_3 hydrocarbons [16].

One very promising class of materials that have been proven to be effective in enhancing the gas separation properties of CA membranes, mostly biogas and flue gas, are ionic liquids (ILs) [17–21]. ILs can potentially produce high-performance gas separation membranes [22]. They are molten salts with low melting points (<100 °C, many below RT) and were first utilized by the U.S. Air Force Academy, in the 1960s, as electrolyte salts for thermal batteries [23]. The most typical types of ILs are salts composed of organic cations, such as tetraalkylammonium $[NR_4]^+$ or tetraalkylphosphonium $[PR_4]^+$, alkylimidazolium $[R_1R_2IM]^+$, alkylpyridinium $[RPy]^+$, paired with various anions such as tetrafluoroborate $[BF_4]^-$, hexafluorophosphate $[PF_6]^-$, methanesulfonate (mesylate) $[CH_3SO_3]^-$, trifluoromethanesulfonate (triflate) $[CF_3SO_3]^-$, nitrate $[NO_3]^-$, and bis-(trifluoromethanesulfonyl)amide $[Tf_2N]^-$, along with several low-melting bromide, chloride, and iodide salts [24,25].

In gas separation, both the cation and anion influence the separation efficiency of ILs. While the anion generally plays a more dominant role, various studies have reported that the cationic structure can also affect the performance of room-temperature ionic liquids (RTILs) [26–29]. For instance, Ortiz et al. [30] reported an increase in propene solubility by changing the cation from $[BMIM][BF_4]$ to $[Bmpy][BF_4]$ although the propene/propane selectivity decreased. In another study [31], an extensive thermodynamic screening was conducted under ambient conditions and low pressure, involving over 20 ILs and their binary mixtures for propene/propane separation. It was observed that increasing the side-chain length on imidazolium cations (a series of 1-alkyl-3-methylimidazolium salts of the type $[RMIM][Tf_2N]$, where R = methyl, ethyl, propyl, butyl) enhanced propene solubility, but led to a decrease in ideal selectivity. Conversely, changing the anion from $[Tf_2N]^-$ to $[DCA]^-$ significantly improved the propene/propane separation. The authors noted that while propene solubility was not strongly influenced by the cation side chain, propane solubility increased with longer alkyl chains, thereby reducing selectivity [31]. Using $[C_2C_1Im]^+$ as a cation, Camper et al. found that propene solubility followed the trend $[Tf_2N] > [DCA] > [CF_3SO_3]$ while the selectivity decreased accordingly

[32]. These findings on the tuneable solubility and selectivity properties of ILs, achieved through structural variations in both cation and anion, have facilitated their application in mixed matrix membranes.

The interaction between ILs and CA has been reported in studies that explored the role of ILs as safe and novel plasticizers [33–35], showing successful gas separation efficiencies mostly for light gases such as CO_2/CH_4, CO_2/N_2, and O_2/N_2 [10,24,25,36–38]. For instance, Lam et al. [39] investigated IL-doped CTA membranes for CO_2/CH_4 separation and they reported a decline in crystallinity and Tg of the polymer both with [EMIM][BF_4] and with [EMIM][DCA], along with an increase in CO_2 absorption and CO_2/light gas permselectivity. These performance improvements are intrinsically linked to the interactions between ILs and the polymer matrix, as demonstrated by extensive research focused on the optimization of cation-anion combinations for cellulose dissolution [40,41], which reveal that anions play a more important role than the cations by disrupting cellulose's hydrogen-bond network through new H-bond formation [42,43]. Cations have weaker effect and may interact with cellulose by the formation of weak H-bonds [44,45] or by Van der Waals interactions [46,47]. Simulations show that the arrangement of the cations also depends on the nature of the anions [48,49]. For instance, Rabideau's simulations of 15 imidazolium-based ILs revealed that the ILs form a patchwork at the surface of cellulose strands, where the anions interact mainly with the hydrophilic sites while cations associate more with the hydrophobic regions of cellulose [50].

Although there are a few works in the literature, considering CA application for C_3H_6/C_3H_8 separation [16,51–54], to the best of our knowledge, no studies have yet established a direct correlation between the transport properties of propene and propane and the tailored physicochemical characteristics of CA, modified with ionic liquids. Recognizing this gap, along with the limited exploration of the blending of ILs with cellulose derivatives for propene and propane separations, this study explored the integration of three imidazolium-based ionic liquids (Scheme 1) into cellulose acetate membranes to systematically investigate their potential not only as plasticizers but also as performance enhancers. The strategy behind selecting these materials was to investigate the effect of anions on tailoring the CA structure, while the cation (BMIM) remained constant to avoid complicating the effects. Imidazolium-based ILs have been widely recognised as successful materials for disrupting the strong hydrogen bonding network in cellulose acetate, leading to a reduction in polymer crystallinity and a desirable plasticising effect [35,38,40,47,55–59]. Along with various physical characteristics, the gas transport properties were initially screened with a series of light gases, and the analysis was then focused on propene and propane. We hypothesise that the incorporation of the appropriate aprotic ionic liquids into CA can sufficiently plasticise the polymer and result in a radical enhancement of the overall permeability yet maintaining a sufficiently high stiffness and mechanical strength to preserve the selectivity, especially for gas pairs like propene/propane that may benefit from both size-selectivity and solubility-selectivity. The results confirm promising improvements in the challenging separation of propene/propane, which is an important step towards cleaner and more energy-efficient olefin purification technologies.

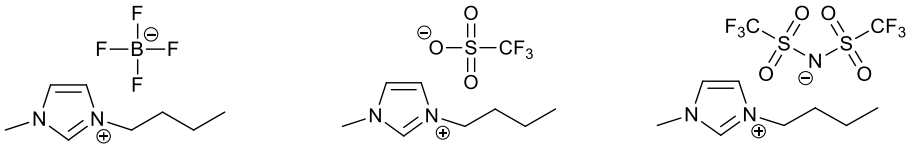

[BMIM]$^+$ [BF$_4$]$^-$ **[BMIM]$^+$ [OTf]$^-$** **[BMIM]$^+$ [Tf$_2$N]$^-$**

Scheme 1. Structure of the ionic liquids used in this work.

2. Experimental

2.1. Material

Cellulose acetate (CA) with the degree of substitution (DS) 2.34, as determined by NMR, was obtained as a gift from SNIA, Italy. The solvents including acetone (98%), Hexane (99.5 %), DMSO-d_6 (Thermo Scientific, 99 atom% D) were obtained from Merck. The ionic liquids (ILs) 1-Butyl-3-methylimidazolium trifluoromethanesulfonate, ([BMIM]$^+$ [OTf]$^-$, $C_9H_{15}F_3N_2O_3S$), 97%, 1-Buty-3-methyl-imidazolium tetrafluoroborate ([BMIM]$^+$[BF$_4$]$^-$, $C_9H_{15}BF_4N_2$), 97%, and 1-butyl-3-methylimidazolium bis (trifluoromethanesulfonyl) imide ([BMIM]$^+$[Tf$_2$N]$^-$, $C_{10}H_{15}F_6N_3O_4S_2$), 98%, were supplied by Merck and Aldrich, respectively. Elastosil ® M4601 (for coverage of the membrane defects), was provided by Wacker Chemie AG. (Munich, Germany). The employed gases for the permeation tests, including O_2, N_2, CH_4, CO_2 with a purity of 99.99+% as well as light hydrocarbons including C_3H_6 (purity > 99.5 %) and C_3H_8 (purity > 99.5%) were obtained from Sapio, Italy. Table SI 1 displays the physical characteristics and molecular structure of the CA and the ILs used in this study.

2.2. Membrane preparation

A 10 wt% stock solution of CA was prepared by dissolving the polymer (previously dried in an oven at 100 °C, overnight) in acetone under magnetic stirring until obtaining a clear and homogenous solution. An aliquot of the polymeric solution was then combined with the ILs, [BMIM]$^+$[OTf]$^-$, [BMIM]$^+$[BF$_4$]$^-$, and [BMIM]$^+$[Tf$_2$N]$^-$, to achieve three distinct concentrations (10%, 20%, and 30 wt.%) for each IL, followed by magnetic stirring at room temperature overnight. The solutions were cast manually on a clean glass plate at 30°C, using a film applicator (Elcometer) with a fixed calibrated casting gap. To minimize the probability of pinhole defects, two successive layers were cast with an interval of 10 minutes at a casting gap of 250 and 100 µm, respectively. The membranes were allowed to dry overnight in a thermostatic chamber at 30°C. Two series of membranes were prepared: the first was coated with a layer of silicone solution to heal any eventual defects and used for permeation tests, and the second series was kept uncoated and used for physical characterizations. The silicone solution was prepared by mixing the two components of the PDMS Elastosil M4601 in the weight ratio 9:1, based on the supplier's instructions, and dissolved in n-Hexane at 25 wt%. A thin film of PDMS solution was deposited onto the membrane surface through dip-coating, followed by a 24-hour resting at room

temperature to ensure complete crosslinking. The list of the membranes and their characteristics is provided in Table SI 1.

2.3. Physicochemical Characterizations

The chemical structure of cellulose acetate, particularly its degree of substitution (DS) with acetate groups, was determined by ^{1}H (500 MHz) and ^{13}C (125 MHz) NMR spectroscopy, using an Avance Bruker DPX 500 (500 MHz) instrument. The NMR analysis was performed on a sample solubilised in DMSO-d6. All the spectra were acquired and processed with TopSpin 3.5 on a Linus PC and analysed with the software Mnova on a Window PC.

The apparent molar mass of cellulose acetate was determined by Gel Permeation Chromatography (GPC), using a Shimadzu Prominence-i GPC System, equipped with a refractive index (RI) and a UV detector. The polymers concentration was set as 2 mg mL^{-1}. Tetrahydrofuran (THF) was used as the eluent and the flow rate was set up at 1.0 mL min^{-1}. The samples were eluted on a Phenogel (5 µm, 10E3 Å) column at 40 °C for 30 minutes. The calibration curve was prepared with polystyrene standards up to 100K.

The crystallinity of the CA raw material and the CA membranes was evaluated via powder X-ray diffraction (PXRD) analysis on a Bruker D2 PHASER diffractometer (2nd generation, Germany), using CuK_{α} radiation (λ = 1.54056 Å). Two CA samples were selected as reference: one sample was kept at ambient temperature, while the other was dried at 100 °C overnight before testing. Data were collected at room temperature in the 2θ range of 2–40°.

The thermal properties of the polymer and the membranes were studied using thermogravimetric analysis (TGA), derivative thermogravimetric (DTG), and differential scanning calorimetry (DSC). TGA and DTG measurements were carried out on a Perkin Elmer TGA 8000 thermogravimetric analyser. Samples of 10-15 mg of the CA membrane, the pure ILs, and the IL-CA MMMs were analysed in the temperature range from 25 to 850°C at a scan rate of 10°C/min, under a dry nitrogen atmosphere. DSC measurements were performed using a Pyris Diamond differential scanning calorimeter (Perkin-Elmer) equipped with an Intra-cooler refrigeration system. To conduct this, 18−20 mg of the samples were weighted and wrapped in a small disk of aluminium foil (~ 6-7 mg), followed by a heating-cooling-heating cycle between 0 °C and 250 °C at a rate of 15 °C min^{-1}. The temperature and heat flow were previously calibrated with indium and zinc standards.

Tensile tests on the membranes were performed by a Zwick/Roell, Universal Testing Machine model Z2.5, single column tensile tester, equipped with a 200 N load cell and curved pneumatic clamps, at 23-25°C, RH:45-50%. The strips were cut with an effective size of 3 cm x 0.5 cm (distance between the clamps and sample width) at a relative deformation rate of 100% min^{-1} for the Young's modulus determination followed by 500% min^{-1} until breakage. The clamp surface and the end parts of membrane strips were covered with adhesive rubber and paper, respectively, to avoid slipping or damaging the softer samples with high IL content.

159 *2.4. Gas transport properties*

160 Gas permeation tests were conducted using a fixed-volume pressure increase device, designed by HZG and
161 built by Elektro & Elektronik Service Reuter in Geesthacht, Germany, as previously discussed [60]. The tests
162 were conducted on the membrane with an effective area of 13.84 cm^2 at ambient temperature, 25 °C, and a
163 feed pressure of 1 bar. Prior to the measurements, the membranes were thoroughly outgassed to eliminate all
164 adsorbed species. This was achieved using a combination of two membrane pumps and a turbo molecular
165 pump (Pfeiffer), ensuring a high-quality and oil-free vacuum ($<< 10^{-3}$ mbar). Moreover, between subsequent
166 measurements, the absorbed gas was totally removed by evacuating the membrane, for a period of at least 10
167 times the time lag of the previous gas. The permeability of gases was tested in the order of O_2, N_2, CH_4, CO_2,
168 C_3H_6, and C_3H_8.

169 The measurements were performed via the so-called time lag method, in which the entire permeation curve is
170 recorded to determine the diffusion coefficients (D) from the initial transient phases via the time lag (Θ), and
171 the permeability coefficient from the steady state pressure increase rate, thorough the intersection of the
172 extrapolated steady state curve with the horizontal axis according to the equation:

$$D = \frac{l^2}{6 \cdot \Theta} \qquad \text{Eq. 1}$$

173 where l is the membrane thickness. The permeability (P), in Barrer (1 Barrer = 10^{-10} cm^3_{STP} cm cm^{-2} s^{-1}
174 $cmHg^{-1}$), was obtained through the slope of the stationary part of the time-lag curve, *i.e.* the curve of the
175 permeate pressure, p_t, as a function of time, as described previously [60]:

$$p_t = p_0 + \left(\frac{dp}{dt}\right)_0 \cdot t + \frac{RT}{V_P \cdot V_m} \cdot A \cdot l \cdot p_f \cdot S \times \left(\frac{D \cdot t}{l^2} - \frac{1}{6} - \frac{2}{\pi^2} \sum_{n=1}^{\infty} \frac{(-1)^n}{n^2} \exp\left(-\frac{D \cdot n^2 \cdot \pi^2 \cdot t}{l^2}\right)\right) \qquad \text{Eq. 2}$$

176 Where p_0 is the starting pressure, which should be negligible, and $(dp/dt)_0$ is the baseline slope representing
177 the instrumental leak flow rate, which should be small but may not be completely negligible for very slow
178 permeating membranes, or in the case of pinhole defects the baseline slope should show Knudsen diffusion
179 and thus depend on the molar mass of the gas alone. p_f indicated the feed pressure, l is the thickness, A shows
180 the exposed surface area of the membrane, and S corresponds to the solubility coefficient. While V_p is the
181 permeate volume, V_m represents the molar volume of the penetrant gas in standard conditions, and R and T are
182 the universal gas constant and the absolute temperature, respectively. In the pseudo-steady state, where $t >>$
183 Θ, Eq. 2 reduces to:

$$P = \frac{V_P \cdot V_m \cdot l}{RT \cdot A \cdot p_f} \cdot \frac{dp}{dt} \qquad \text{Eq. 3}$$

This enables the direct calculation of the permeability coefficient. Considering the validity of the solution-diffusion model, in which the pressure and concentration are independent transport parameters, the solubility S (m^3_{STP} m^{-3} bar^{-1}) can be indirectly obtained via the ratio of permeability and the diffusion coefficient:

$$S = \frac{P}{D} \qquad \text{Eq. 4}$$

3. Results and Discussions

3.1. Membrane preparation

3.1.1.Nuclear magnetic resonance (NMR) spectroscopy and Gel Permeation Chromatography (GPC).

Before preparation of the membranes, the degree of acetylation of cellulose acetate was determined by NMR spectroscopy and the molar mass of the polymer was determined by GPC. Figure SI 1a shows the ^{13}C NMR spectrum of the pristine CA powders while Figure SI 1b shows the quantitative ^{1}H spectrum, displaying the integral values for both ^{1}H regions. Based on Figure SI 1a, the observed peaks at 99.71 and 62.98 ppm could be correlated to C_1 and C_6, as reported in the literature [61]. The spectral peaks at 78–70 ppm represent the C_2–C_5 resonances but cannot be further assigned because they exhibited complicated and overlapped spectral lines.

The ^{1}H NMR spectrum is available in Figure SI 1b, showing a complex convolution of peaks corresponding to the acetyl protons. There are three main peaks at 2.07, 1.94 and 1.87 ppm, and some additional ones, due to the different possible acetylation positions, could be observed in this region. This is in agreement with the report of Goodlett et al., who assigned the peaks at 2.09, 1.99, and 1.94 to the acetyl group in the 6-postion, and the hydroxyl groups in the 2- and 3- positions, respectively [62]. In addition, the resonances (or peaks) observed in the region between 5.1 and 3.7 ppm correspond to the 7 protons within the anhydroglucose unit [62]. Using this value as a reference, it was determined that the area of the peaks in the acetyl region accounts for 7 protons. Therefore, considering that each acetyl group has 3 protons, the average number of acetyl groups per ring unit is 2.34 (7/3), which corresponds to a DS of 2.34. This method was precisely reported in Ref. [63].

GPC analysis of the polymer in THF and with polystyrene calibration standards revealed a rather narrow molecular weight distribution (Figure SI 2) with the following characteristics: apparent Mn = 79.9 kg mol^{-1}, Mw = 92.0 kg mol^{-1}, Mz = 102.7 kg mol^{-1}, Dispersity (Đ) = Mw/Mn = 1.15.

3.1.2.Membrane preparation and appearance

All the prepared membranes showed a transparent and homogenous appearance (Figure SI 3). Compared to the neat CA membrane, the IL-blended CA membranes showed higher flexibility, and they were removed more easily from the glass plate once the membrane formation was completed. The latter means a lower risk of introducing defects by mechanical stresses needed for peeling the membrane from the support, which occasionally occurs during the separation of the membranes from the glass support. This indicates the

effectiveness of the ILs in decreasing the rigidity of the CA membrane, especially for those containing $[BMIM]^+[Tf_2N]^-$. Figure 1 shows the SEM top and cross-section images of the neat CA and 30% IL-CA blended-membranes. All membranes exhibited a quite uniform, dense, and defect-free appearance, except for the neat CA membrane, which shows a few localized pores in its cross-sectional area (Figure 1a). The slightly porous morphology of this neat CA membrane could originate from the rigid structure of CA that may not have tolerated the tensions imposed during the membrane preparation for SEM analysis. Instead, the sample with 30% $[BMIM]^+[BF4]^-$ exhibited a completely uniform appearance (Figure 1b) and felt almost rubbery. The same effect was also observed in the case of 30% $[BMIM]^+[OTf]^-$-CA and 30% $[BMIM]^+[Tf_2N]^-$ -CA blended-membranes (Figure 1b-c) confirming the plasticizing effect of these ILs.

3.2. Membrane characterization

Crystallinity provides thermal and mechanical stability to polymers but also resistance to gas transport, as crystalline regions are usually not permeable or less permeable than the amorphous phase of polymers, with very few rare exceptions such as syndiotactic polystyrene [64,65] and poly(2,6-dimethyl-1,4-phenylene) oxide (PPO) [66]. Therefore, these properties are all highly important for the evaluation of gas separation membrane performance.

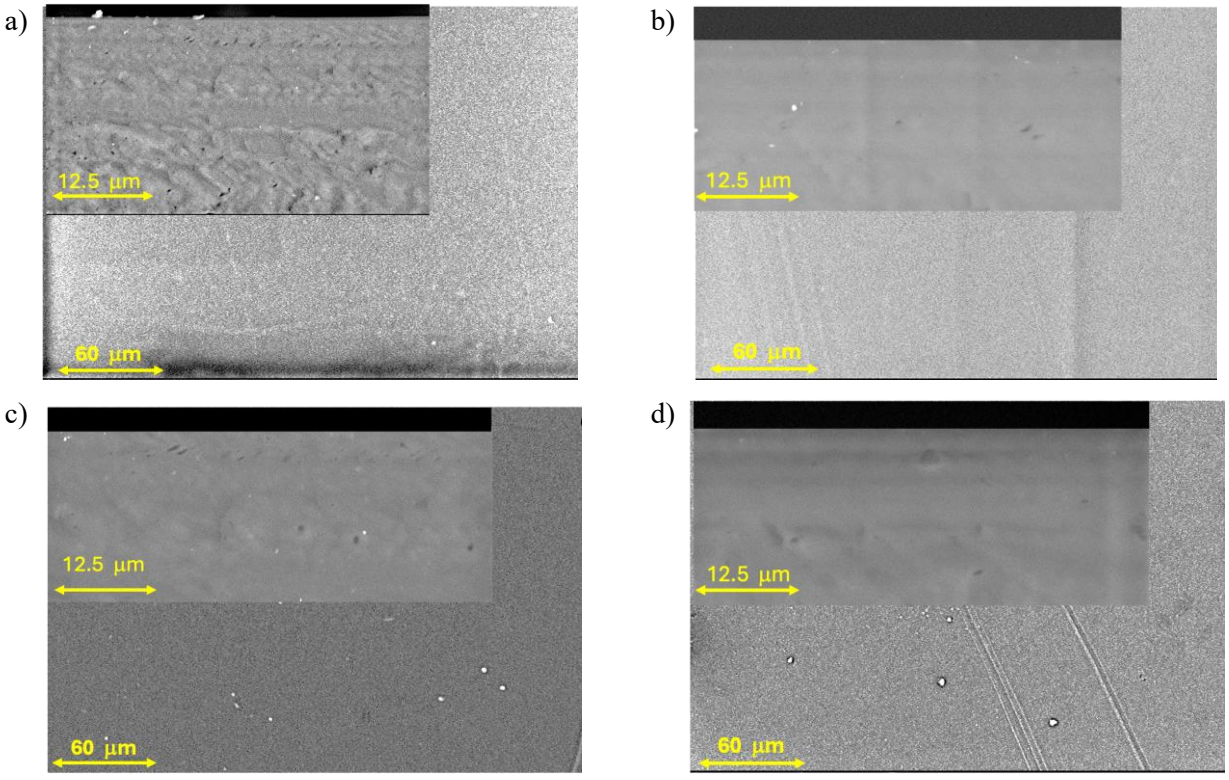

Figure 1. Top and cross-sectionals (inset) SEM images of a) neat membrane, b) 30% $[BMIM]^+[BF_4]^-$-CA c) $[BMIM]^+[OTf]^-$-CA and d) $[BMIM]^+[Tf_2N]^-$ -CA blended-membranes. The cross-section images and top surface images were captured at 3000x and 500x magnifications, respectively.

3.2.1.X-ray diffraction (XRD)

Figure 2 illustrates the XRD pattern of pure CA and that of the membranes with different contents of IL investigated in this study. According to the literature [67], the XRD pattern of a raw CA consists of three distinct peaks at 2θ= 7.5°, 11°, and 14°, representing the crystalline domains, and a broad peak at around 2θ= 18°, relating to the amorphous phase. However, a comparison between the neat membrane spectrum and that of the raw CA powder samples reveals that the membrane fabrication process shifted the semi crystalline structure of CA powders to an almost amorphous form, as indicated by the presence of two broad peaks at 2θ= 7.5° and 18°, corresponding to the crystalline and amorphous fractions of CA, respectively [21,68,69]. This could be attributed to the physical stresses that CA underwent during casting or, more likely, to the effects of the solvent (acetone), which promoted the formation of new interactions between CA functional groups (acetyl groups) and acetone, delaying the crystal nucleation and growth. This idea confirms the dissolubility theory of semi-crystalline CA in a solvent that follows two steps: (1) cellulose collapse to an amorphous polymer and (2) disentanglement of the polymer chains for dissolution in the solvent [70].

Figure 2b-d illustrates the inclusion of the ILs within the CA polymeric matrix, which further reduced its crystallinity, as illustrated by the two broader peaks with weakened intensity. This is suggestive of the disruption of essential bonds, such as hydrogen bonds among the OH, esters, and ether oxygen groups [23,47,59] of CA chains. Likely, the formation of new weak interactions established between the CA polymeric matrix and the ILs disrupts the interchain interactions active in the pristine CA, leading to the transition of the CA structure from semi-crystalline to amorphous. Compared to $[BMIM]^+[Tf_2N]^-$ which caused minimal changes, increasing the IL content in the $[BMIM]^+[BF4]^-$ and $[BMIM]^+[OTf]^-$ containing membranes resulted in a constant reduction in peak intensity compared to neat CA, maintaining the structure amorphous.

a) Neat

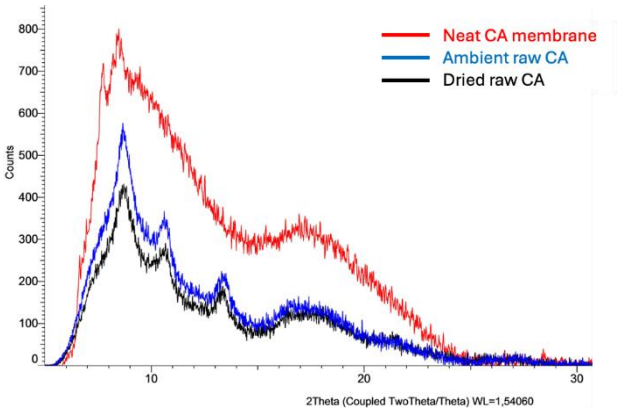

b) $[BMIM]^+[BF_4]$

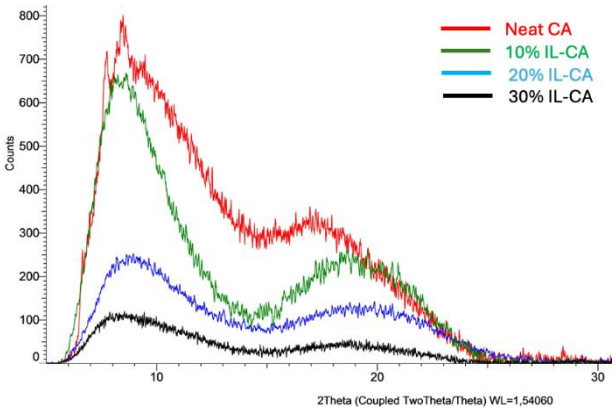

c) $[BMIM]^+[OTf]^-$ d) $[BMIM]^+[Tf_2N]^-$

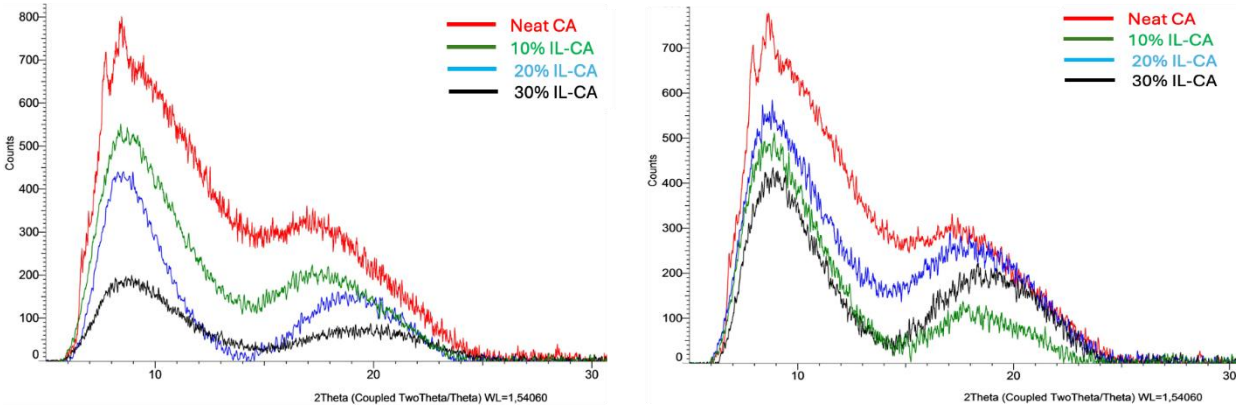

Figure 2. PXRD curves of a) CA powder samples (the one kept at an ambient temperature and that dried at 100°C, overnight) and the neat CA membrane; MMMs consisted of b) $[BMIM]^+[BF_4]^-$, c) $[BMIM]^+[OTf]^-$ and d) $[BMIM]^+[Tf_2N]^-$ series.

3.2.2. Thermal Properties (TGA, DSC analysis)

Analysis of the thermal stability of the neat CA, the pure ILs and the CA/IL membranes by TGA measurements (Figure 3) reveals that the grade of neat CA used in this work degrades above 250 °C. The TGA trace shows a small weight loss below 100°C (Figure SI 4a), most likely due to the loss of humidity and/or residual casting solvent contained within the membrane. These two steps (dehydration and thermal decomposition) occur analogously in the spectra of the pure ILs, except for $[BMIM]^+[Tf_2N]^-$, for which the first dehydration step is not appreciable (Figure SI 4b-d). This is probably due to a more hydrophobic nature of the $[Tf_2N]^-$ anion [71] compared to $[BF_4]^-$ and $[OTf]^-$, which in turn impart a less hygroscopic character to the IL [70]. Moreover, the ILs showed higher thermal stability than CA with a decomposition temperature above 440°C and the onset of degradation above 350°C.

TGA traces of IL-CA membranes (Figure 3 and Figure SI 5-Figure SI 7) display three successive processes which related to the dehydration of the membrane, the decomposition of CA, and the decomposition of the ILs, particularly their imidazolium ring [23], respectively. As a general trend, compared to the neat CA membrane, the ILs slightly decreased the onset of the dehydration process, which is also accompanied by a slight decrease in the percentage of the sample weight lost, due to a reduced amount of the entrapped water molecules within the ILs doped membranes. For all three series, the additives slightly reduced the thermal stability of CA, possibly by a weak catalytic action of the ionic species that accelerate degradation reactions, combined with a reduction of the internal cohesion forces between the polymeric chains (i.e. most probably the interchain H-bonds, the dispersion interactions and hydrophobic effects) [72]. As previously stated, the last registered step on all IL-doped -CA membranes related to the decomposition process of the IL dopant, and its corresponding weight loss agrees with the molar ratio of the dopant utilized. In any case, the onset of degradation takes place at much higher temperature than that at which the membranes would normally be used in practical applications, and therefore the thermal stability of the membranes should not be a problem.

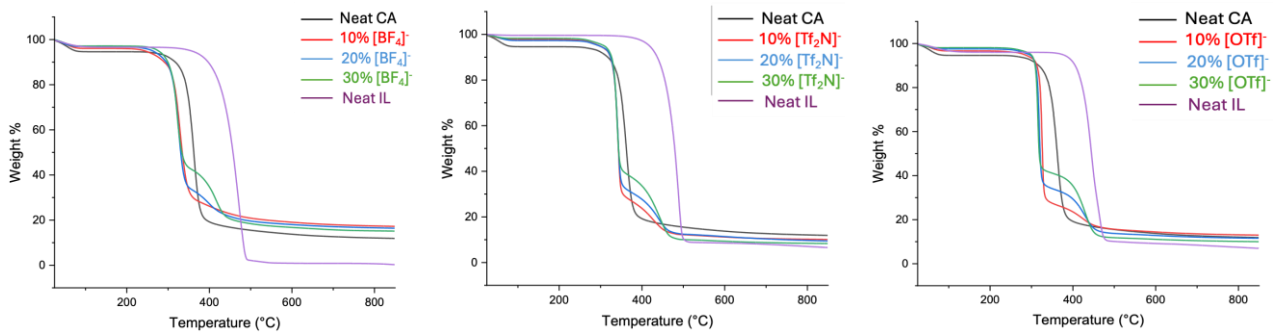

Figure 3. Overview of the TGA results of the CA/IL blend-membranes in comparison with the neat polymer and the pure ILs.

In addition to the TGA results, DSC analysis revealed a plasticizing effect of the ILs on the CA structure. The results are summarized in Figure 4 and Figure SI 9. The glass transition temperature (T_g) of the present grade of CA is ca. 190-195 °C, in agreement with the literature [73], and it has a small melting peak with a maximum at ca. 225°C, being in line with the weakly crystalline character observed by XRD. Figure 4a and b show a consistent decrease in T_g and T_m as the IL content in the blended membranes increases. A similar decreasing trend is observed in the graph of ΔC_p (specific heat) and ΔH_m (melting enthalpy) versus the IL content, Figure 4c-d. This reflects the disrupting effect of these ILs, previously observed in XRD, indicating that the presence of the IL gives rise to membrane less crystalline and more disordered.

a)

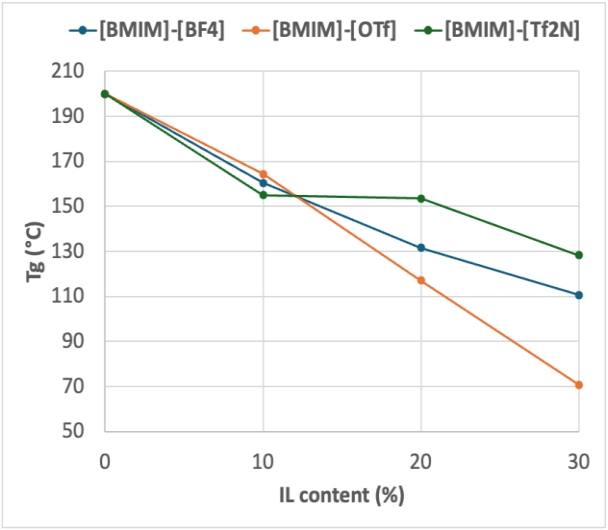

b)

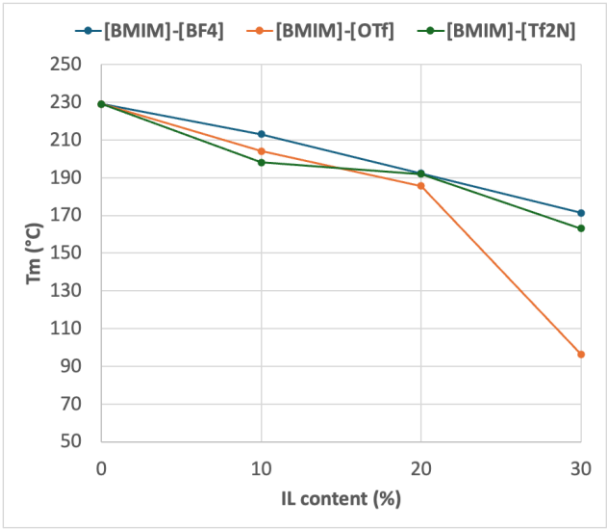

c)

d)

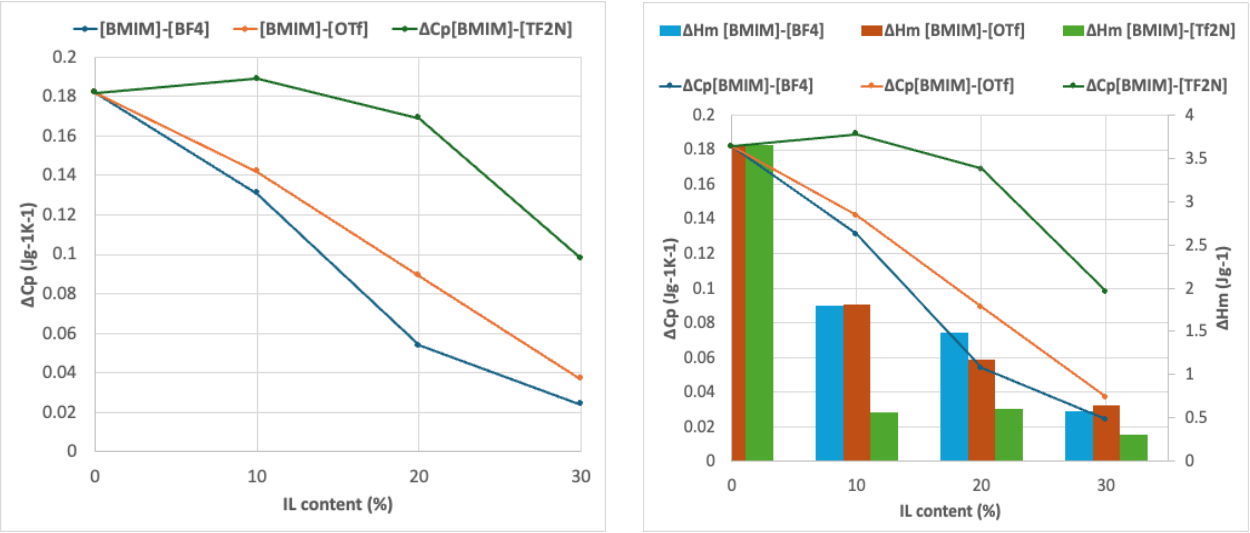

Figure 4. Overview of the thermal properties of the MMMs in comparison with the neat polymer, a) T_g, b)T_m ,c) ΔC_p, d) ΔC_p and ΔH_m. Only the characteristics of first heating is provided. The T_g is reported as the value at half ΔC_p.

Figure SI 9 and Table SI 2 illustrate the changes in thermal properties of each IL-CA membrane based on the IL content for the first heating, first cooling, and second heating cycles. Similar trends have been observed for several other blends of ILs in glassy and semi-crystalline polymers [73,74], and this is a typical effect of ILs, for instance in poly (VDF-*co*-HFP) [75], Pebax [76,77], and PEOT-PBT [78], where the ILs were explored to increase the permeability of the original polymer. Summarizing, for all the IL-containing membranes, the T_g and T_m of the CA membranes gradually decreased with increasing IL content with the largest decrease for $[BMIM]^+[OTf]^-$ and the smallest for $[BMIM]^+[Tf_2N]^-$. At the same time also the overall crystallinity of the sample decreased. Interestingly, it must be noted that all as-prepared samples, as well as the original CA powder, showed a large endothermal peak around 50-100 °C (Figure SI 8), related to the evaporation of absorbed humidity or residual solvent, up to 220 Jg^{-1}. Considering an enthalpy of vaporization of water equal to 2.26×10^3 Jg^{-1} at its boiling point, and somewhat higher at lower temperatures and likely even higher for water trapped inside the membrane matrix, this corresponds to less than 10% water in the samples. This is not far from the 6% weight loss of pure CA membranes determined experimentally by TGA measurements. The humidity could be easily removed by vacuum drying of the sample (Figure SI 8b). An important conclusion from this study is that for the final application of the membrane, the glass transition temperature will be the limiting factor rather than the chemical stability determined by TGA, because above T_g the samples will lose most of their mechanical stability, unless the membranes will be applied as thin film composites on a resistant porous substrate.

3.2.3.Mechanical Properties

For a further evaluation of the mechanical stability of the membranes, tensile tests were performed on all samples. Figure 5 illustrates the results for Young's modulus, the tensile strength and the maximum deformation as a function of the ionic liquid content. Somewhat analogous to the T_g, Young's modulus and

the tensile strength of the blend membranes containing $[BMIM]^+[BF_4]^-$ and $[BMIM]^+[OTf]^-$, show a similar gradual decrease (Figure 5a-b, respectively). Furthermore, in agreement with the DSC and XRD observations, there is a much smaller decrease in Young's modulus of the $[BMIM]^+[Tf_2N]^-$-CA blend-membranes than that of the membranes with other ILs, particularly $[BMIM]^+[BF_4]^-$. Therefore, up to 30% of $[BMIM]^+[Tf_2N]^-$ caused almost negligible changes in the rigidity of the membranes. Noteworthy, the conditions under which mechanical properties and glass transition temperatures are measured differ significantly, since tensile tests are performed at room temperature and 45-50% RH, while DSC is conducted under an N2 flow at temperatures above 180 °C. This difference in temperature and in RH strongly influences the CA-CA, CA-IL and CA-H2O interactions (especially polar interactions and hydrogen bonds), which, in turn, affect the thermal and mechanical properties. In addition, these methods probe different aspects of the material: mechanical tests reflect bulk elasticity, while Tg represents molecular-level segmental mobility. This explains why ILs may affect them differently and why results from the two techniques may not directly correspond. In any case, even at the highest IL content of 30 wt%, all membranes exhibit an elastic modulus of several hundreds of MPa, in the typical range of stiff glassy polymers.

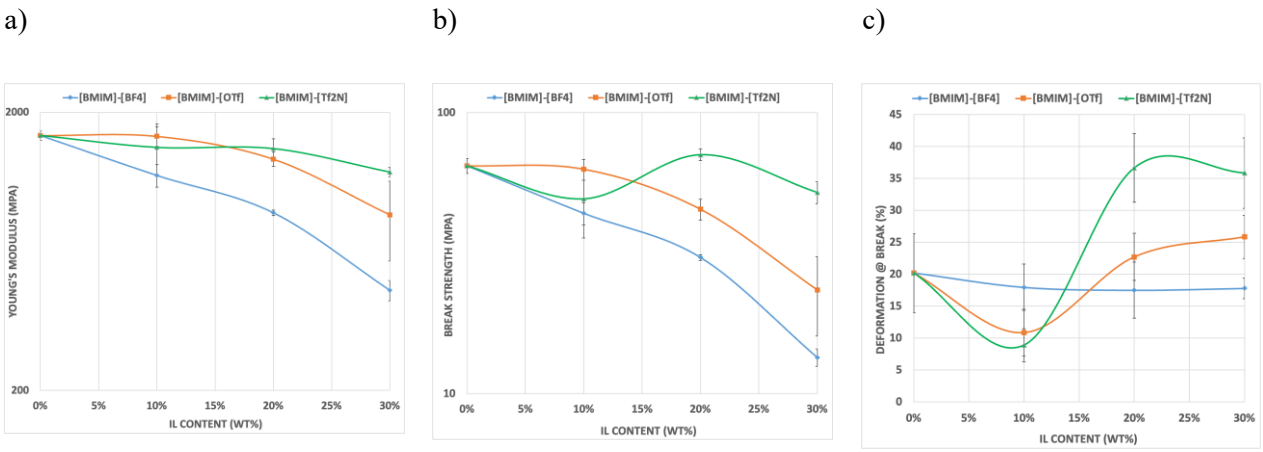

Figure 5. a) Young's modulus, b) tensile strength and c) maximum deformation of the CA/IL samples with different amounts of $[BMIM]^+[BF_4]^-$ (●), $[BMIM]^+[OTf]^-$ (■) and $[BMIM]^+[Tf_2N]^-$ (▲). Averages and standard deviation of 4-6 samples. The lines are indicated as a guide to the eye.

The tensile strength shows roughly the same trend as Young's modulus. Thus, although the IL does indeed plasticize the polymer to some extent, the membranes are expected to withstand high pressures without major problems. The absolute value of the elastic modulus and tensile strength depends mostly on the affinity of the IL with the CA polymer matrix. This is generally good for all three ILs, giving visibly homogenous transparent films (Figure SI 3d), but the difference between the three series depends on the delicate balance between the polymer-polymer, the polymer-IL and the IL-IL interactions. Figure 5c shows the maximum deformation, which represents the mechanical resistance to stretching or the elasticity of the blended-membranes versus the IL content. This illustrates a relatively stable deformation at break by increasing $[BMIM]^+[BF_4]^-$ content, indicating that the ductility of the material remains similar, regardless of the increasing IL content. In contrast,

[BMIM]$^+$[OTf]$^-$-CA and [BMIM]$^+$[Tf_2N]$^-$ exhibited a significant oscillation. If this is truly representative for these materials is not clear, because in this range the stress-strain curve is nearly horizontal, and a slightly higher or lower tensile strength determines a major change in maximum deformation. This may be due to subtle differences in the sample morphology, or to the presence of imperfections in the test specimen, such as micro-bubbles included during casting, or roughness introduced into the test sample during cutting, which may trigger early rupture.

In summary, the results of the physical characterizations indicate that the addition of the ILs led to a reduction in CA's thermal stability, stiffness, and crystallinity while it generally increased the flexibility and elasticity of the blend-membranes. This can be attributed to the plasticizing effect of the ILs and the associated changes in the CA structure, as also reported in the literature [79].

It is widely accepted that the crystallization of CA chains is driven by supramolecular forces such as hydrogen bonds and van der Waals forces [17]. ILs can act as good electron-donor and hydrogen bond acceptors upon interaction with the oxygen and hydrogen atoms of CA-OH, the anion of IL generally acts as a proton acceptor, whereas the cation behaves as an electron acceptor [80,81]. The collapse of the crystalline domains is most likely due to the breaking of the hydrogen bonding interactions among the CA chains [81]. On the other hand, the IL molecules could act like lubricants among CA chains, facilitating the mobility of CA [82]. This mechanism is evident in the membranes containing [BMIM]$^+$[BF_4]$^-$ molecules which possess spherical shape and less polar structure, the lowest molecular weight (MW), and the highest viscosity, compared to the other studied ILs, observable in Table SI 1. On the other hand, [BMIM]$^+$[Tf_2N]$^-$ possesses the most branched and polar structure compared to the other two ILs. It also possesses the highest MW and the lowest viscosity which make it a good candidate for forming slightly stronger and more intimate interactions with CA molecules. Moreover, based on the free volume theory [83], [BMIM]$^+$[Tf_2N]$^-$ can extend the free volume in the CA 3D network by dedicating more end groups and side chains to the CA structure. This could be intensified by its low viscous characteristics as it could move better among CA chains and can access more unbonded functional groups that act as a plasticizer at more diluted solutions of CA and [BMIM]$^+$[Tf_2N]$^-$, 30%.

Furthermore, [BMIM]$^+$[OTf]$^-$ showed intermediate performance compared to these two ILs since it benefits from both possessing relatively small molecules that facilitate its performance as a lubricant, obvious from its T_g and good mechanical flexibility, which was mostly close to [BMIM]$^+$[BF_4]$^-$ behavior. It contains more functional groups and a more polar structure than [BMIM]$^+$[BF_4]$^-$ but less than [BMIM]$^+$[Tf_2N]$^-$, which candidate it to increase the number of weak interionic interactions with CA molecules especially when its content increased from 10% to 30% wt.

3.3. Gas Permeation Analysis

The transport properties of the membranes were evaluated by pure gas permeability measurements in the time lag mode, which continuously records the permeate pressure from the initial exposure of the membrane until achieving a steady state in the gas permeation. Due to the low intrinsic permeability of CA and thus the very

low permeate flow rate, the leak flow rate (instrumental and through pinholes) was not completely negligible (e.g. Figure SI 10-b) and in some cases even dominant (e.g. Figure SI 10-a). Therefore, the membranes were routinely coated with silicone sealant. This resolved the problem of the pinholes (Figure SI 10-c,d) but for gases such as propene and especially propane with an extremely low permeability and very slow diffusion, and thus very long measurement times, even after silicone coating the baseline slope was not completely negligible because of the low but measurable instrumental leak flow (Figure SI 11-c,d). The residual baseline was measurable accurately and could, fortunately, be completely corrected by subtracting the term and $(dp/dt)_0$ in Eq. 2. Assuming the validity of the solution-diffusion model, the solubility (S) and diffusivity (D) coefficients are two intrinsic transport properties of the membrane that identify the permeability coefficient (P) by their product and thus determine the overall potential of gas molecules to permeate through the membrane [84]. Figure SI 12 follows the changes in P, D, and S of the studied gases during their permeation across the CA-based blended-membranes based on the IL content. With increasing content of all three ILs, the permeability shows a generally increasing trend for all gases (CO_2, N_2, CH_4, C_3H_6, and C_3H_8), which is mainly due to the increase in diffusivity, whereas the solubility tends to decrease at higher IL content (Figure SI 12). A somewhat more detailed discussion on the CO_2/CH_4, CO_2/N_2 and C_3H_6/C_3H_8 separations is reported below.

3.3.1.Pure gas permeability and ideal selectivity of the CO_2/CH_4 and CO_2/N_2 gas pairs

While Figure SI 12 illustrates the changes in the transport properties of the desired gases in CA blended-membranes as a function of the IL content, Figure 6a and b shows the CO_2 permeability and CO_2/CH_4 and CO_2/N_2 ideal selectivities of the blended-membranes. Compared to the neat CA membrane, adding $[BMIM]^+[Tf_2N]^-$ up to 30% resulted in a constant enhancement in the CO_2, CH_4, and N_2 permeability but CO_2/N_2 and CO_2/CH_4 selectivity reduction (Figure SI 12 and Figure 6a-b). This obvious plasticization effect is correlated with other physical characteristics.

Analogously, adding $[BMIM]^+[BF_4]^-$ and $[BMIM]^+[OTf]^-$, up to 20%, generally enhanced the permeability of all the studied gases, mainly because of their diffusivity improvement, but decreased the CO_2/CH_4 and CO_2/N_2 ideal selectivity according to the well-known trade-off behaviour. This usual plasticization effect of the ILs is in agreement with the lower T_g and lower Young's modulus, observed via DSC and tensile tests. Nevertheless, adding more of these ILs led to only CO_2 permeability increase but declined CH_4 and N_2 permeability and diffusivity (Figure SI 12), leading to a jump in CO_2/CH_4 and CO_2/N_2 ideal selectivity at 30% $[BMIM]^+[BF_4]^-$ and $[BMIM]^+[OTf]^-$, compared to what achieved by 20% content. It must be noted that the transport parameters are the effective values, and since the crystalline phase is generally not permeable, the effective permeability, P_{eff}, is lower than that of the continuous amorphous phase, P_d, according to the Maxwell equation:

$$P_{eff} = P_c\left[\frac{P_d + 2P_c - 2\Phi_d(P_c - P_d)}{P_d + 2P_c + \Phi_d(P_c - P_d)}\right] \quad \text{Eq. 5}$$

where Φ_d is the volume fraction of the dispersed phase, i.e. the crystallinity. Φ_d was calculated with an impermeable dispersed phase, where $P_d = 0$.

$$P_{eff,min} = P_c\left[\frac{1-\Phi_d}{1+0.5\Phi_d}\right] \qquad \text{Eq. 6}$$

Similarly, also the diffusion coefficient is lower than that of the amorphous phase although situations may exist where the apparent diffusion coefficient is, by time lag measurements, higher in MMMs with impermeable particles than in the neat polymer [85]. Therefore, the final trend depends on the crystallinity, the degree of plasticization and changes in gas solubility, and the trend may not be fully linear and predictable. Indeed, in many polymers the increased CO_2 permeability is attributed to a higher solubility of CO_2 in the polymer matrix, but this is not observed in this case. Besides the possibly inaccurate indirect calculation of the solubility, by the reasons outlined above, the very strong affinity of the polar ILs with the CA, reduces the solubility of the lighter gases in the latter. Normally, the affinity of CA to absorb CO_2 is attributed to the -OH groups in cellulose molecules, providing adsorption sites for enhanced carbon capture [86]. Interaction with the dipole moments of polar functional groups such as -OH groups and carbonyl (C=O) and ester groups in the CA structure induce a dipole in the quadrupolar CO_2 molecules which generally leads to higher absorbance and enhanced permeance of CO_2 compared to CH_4 and N_2. Investigating the effect of different ILs, Muldoon et al. [86] expressed that both cations and anions effectively control the CO_2 solubility in the ILs, although the anion plays the most critical role. They showed that in $BMIM]^+$-based ILs at 60 °C, the order of CO_2 solubility is $([NO_3]^-) < ([BF_4]^-) < ([DCA]^-) \sim ([PF_6]^-) \sim ([TfO]^-) < ([Tf_2N]^-) < ([methide]^-)$. This subject was also supported by Kanakubo et al. [87] via performing X-ray diffraction study, suggesting that the anions with the most fluorinated fluoroalkyl groups have the highest CO_2 solubilities. Aki et al. came to a similar conclusion for a series of [alkylimidazolium][Tf_2N] and [alkylimidazolium][Methide] ionic liquids where the increase in the alkyl chain length on the cation affects the CO_2 solubility only marginally, compared to the effect of the anion [88] while Hojniak et al found a stronger effect of the RTIL cation on the CO_2/N_2 and CO_2/CH_4 selectivities in SILMs, in particular when comparing dicationic and monocatonic ILs [89]. This is in agreement with the results obtained in this work as the CO_2 solubilities which obtained via the time-lag method showed 1.32 $cm^3_{(STP)}\,cm^{-3}\,bar^{-1}$ for 30% $[BMIM]^+[Tf_2N]^-$, in contrast to 1 $cm^3_{(STP)}\,cm^{-3}\,bar^{-1}$ for 30% $[BMIM]^+[BF_4]^-$.

Summarizing, the effect of the ILs on the transport of light gases is a complex combination of specific microsctructural and physico-chemical properties for each IL. Generally, the incorporation of ILs leads to decreased crystallinity and increased chain mobility, evidenced by a reduction in glass transition temperature (T_g) and Young's modulus. While the effect at 10 wt% or 20 wt% may be ambiguous, at 30 wt% the plasticization dominates the permeability and especially the diffusivity, which are always higher than that in the neat CA. Similar results were observed in the literature [21,25,90]

425

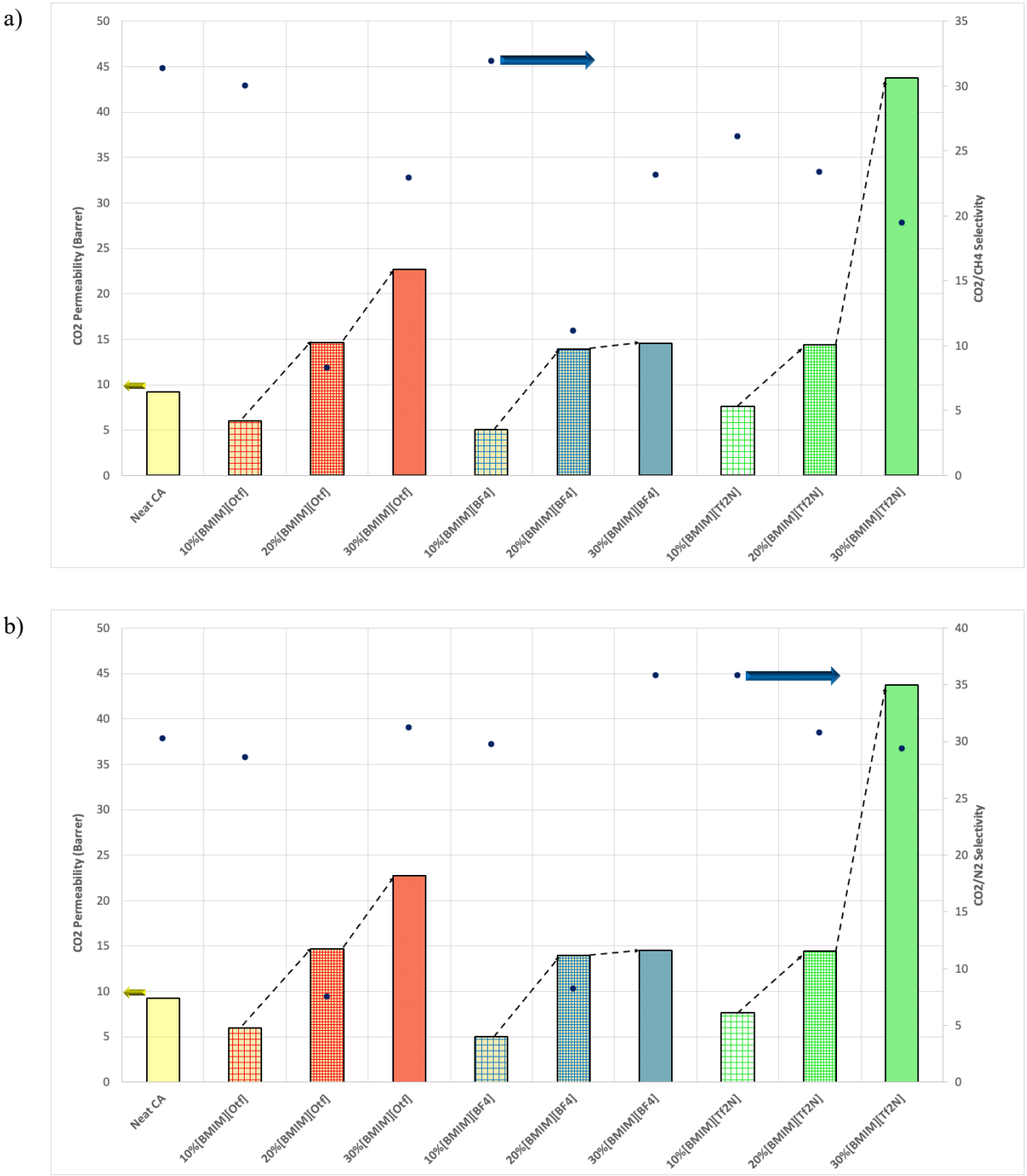

Figure 6. Permeability (bar chart, left axis) and ideal selectivity (blue dots, right axis) of CA-based membranes with different contents of the ILs for a) CO_2/CH_4 and b) CO_2/N_2 gas pairs. The gas transport data of membranes represented by (yellow for the neat, red for $[BMIM]^+[OTf]^-$, blue for $[BMIM]^+[BF_4]^-$, and green for $[BMIM]^+[Tf_2N]^-$.

426 3.3.2. C_3H_6/C_3H_8 Pair

427 Despite the almost prohibitively slow permeation of C_3H_6 and C_3H_8 through a neat CA membrane (Figure SI
428 11), the observed trends with a) CO_2/CH_4 and b) CO_2/N_2 permeation and diffusion as a function of the IL

content led us to measure nevertheless the C_3H_6 and C_3H_8 transport properties of the MMMs containing 30% of the ILs. As illustrated by the Robeson plot in Figure 7, the ILs have a very positive effect on the permeability of C_3H_6 in all membranes compared to the neat CA, with a nearly 50x increase for $[BMIM]^+[Tf_2N]^-$. Moreover, except for the $[BMIM]^+[BF_4]^-$-CA blends, which showed the same selectivity as the neat CA membrane, the membranes with both the other ILs interestingly achieve a higher C_3H_6/C_3H_8 ideal selectivity, particularly that with $[BMIM]^+[Tf_2N]^-$. This is observable in Figure SI 13, displaying the time lag curves of 30%ILs-CA blended-membranes which confirms the improvement of the permselective properties of the membranes is mainly due to enhanced diffusivity. All the ILs significantly showed shorter time-lag periods for both gases, in the order of $[BMIM]^+[Tf_2N]^-$ < $[BMIM]^+[OTf]^-$ < $[BMIM]^+[BF_4]^-$ << Neat CA membrane. The 30% $[BMIM]^+[Tf_2N]^-$-CA blended membrane achieved a time lag of 103s and 243s for propene and propane, respectively, corresponding to 73x and 65x faster diffusion compared to the neat CA. This could be attributed to the "gas carrier" characteristics of the ILs, which enhance the gas transfer solution-diffusion mechanism. Here, as illustrated in Scheme 1 and Table SI 1, $[BMIM]^+[Tf_2N]^-$ contained the largest anion and exhibited better performance in improving the gas transport. The higher propene/propane selectivity achieved by $[BMIM]^+[Tf_2N]^-$ (~5), compared to other ILs, 4 for $[BMIM]^+[OTf]^-$ and 3.5 for $[BMIM]^+[BF_4]^-$, was also reported by Wang et al. [91], who worked on a nonporous composite polymer made from thermoplastic polyurethane (TPU) and several silver salts with ILs, and Vu et al., who studied a system of IL-layered ZIF-67 particles incorporated into 6FDA-durene polymer [92].

This plasticization effect of the ILs, particularly the branched $[BMIM]^+[Tf_2N]^-$, can be also observed in Figure SI 12, which depicts an enhanced permeability and diffusivity of both propene and propane. The membranes, nevertheless, maintained significant size-selective characteristics to favour the smaller diameter of the C_3H_6 molecules than C_3H_8 molecules, resulting in a shorter time lag (Figure SI 12) *i.e.* faster diffusion of propene compared to propane (Figure SI 12b,e,h). Furthermore, propene possesses π-bonds, which boosts its affinity towards CA and ILs, leading to efficient separation of this gas from propane by the present membranes due to a higher solubility (Figure SI 12c,f,i).

Figure 7 provides the Robeson plot [1], and Table SI 3 lists the numerical permselectivity data of this work in comparison with other cellulosic polymers reported in the literature [16,51,52,54,93,94]. To evaluate the performance of our membranes we used the Robeson upper-bound reported by Koros et al. for this separation [1]. Based on that, for the 30 wt% $[BMIM]^+[Tf_2N]^-$/CA blended-membrane displayed amongst the highest selectivities of cellulosic polymers, while maintaining a reasonable permeability for C_3H_6. This is a noticeable result, suggesting that by employing an appropriate concentration of a compatible IL, it is possible to tailor the CA structural, thermomechanical and transport properties, to achieve both an enhanced C_3H_6 permeability and a higher C_3H_6/C_3H_8 selectivity. It is worth to highlight again that it is very challenging to achieve an improvement in both the propene permeability and its selectivity over propane because of their close kinetic diameter, particularly when a glassy polymer such as CA is employed, which normally shows low propene permeability and trade-off perm-selectivity behavior.

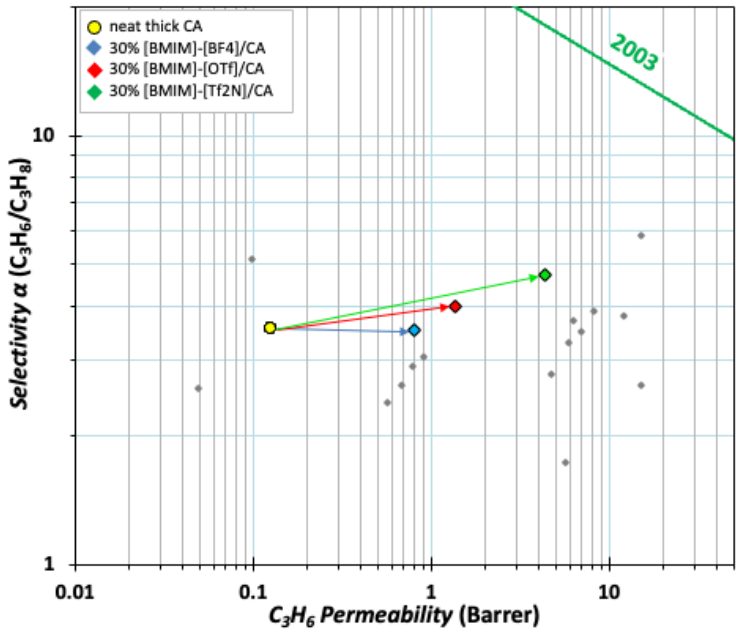

Figure 7. Perm-selectivity trade-off (Robeson plots) for different couple of gases of CA-based membranes with 30% contents of the ILs. The gas transport data of membranes represented by (yellow for the neat, blue for 30% $[BMIM]^+[BF_4]^-$, red for 30% $[BMIM]^+[OTf]^-$, and green for 30% $[BMIM]^+[Tf_2N]^-$. The gray points refer to values for cellulosic polymers from the literature [16,51,52,54,93,94]

3.3.3. The correlation of Diffusivity based on an Effective Diameter

To gain a clearer understanding of the gas permeation mechanism in the blended membranes, Figure 8 shows the relationship between a gas diffusivity and its effective diameter. It has been established that the diffusion coefficient (D) of the penetrant correlates with the square of the effective gas diameter, the smaller the gas effective diameter the faster the gas diffusivity [95], especially for highly rigid polymers [96]. This trend was observed in all the gases studied and only CO_2 showed a small negative deviation from the trend, which could be related to the specific affinity of CO_2 for the polymer matrix. The correlation with the square of the effective diameter is explained by the fact that the resistance to transport depends on its cross-sectional area. Accordingly, among the gases analysed, propene and propane exhibited the lowest diffusivity, because they have the largest molecular sizes. Furthermore, Figure 8 shows that the addition of the ILs increased the D values, indicating that IL-CA blended-membranes could facilitate the gas permeation, especially for C_3 hydrocarbons, with the order of 30% $[BMIM]^+[Tf_2N]^-$>30%$[BMIM]^+[OTf]^-$>30% $[BMIM]^+[BF_4]^-$. The reduction of the slope of the trend line upon the addition of the IL confirms that the size-selectivity decreases.

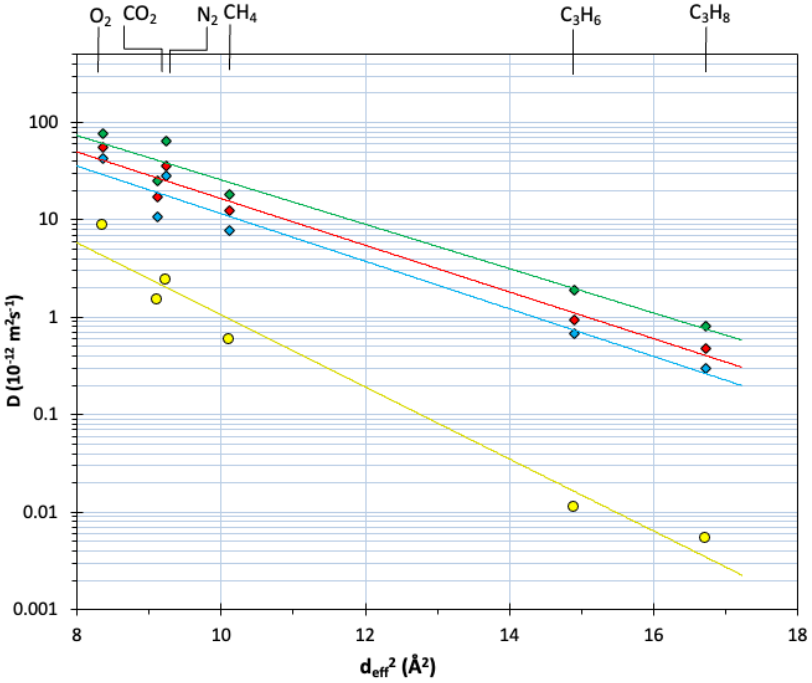

Figure 8. Correlation of D and d^2_{eff} for CA with a) $[BMIM]^+[BF_4]^-$, b) $[BMIM]^+[OTf]^-$, and c) $[BMIM]^+[Tf_2N]^-$. The diffusion data of the neat CA membrane are shown by yellow circles (●) while diamonds represent the membranes with 30% of the ILs. Color code: red (◆) for $[BMIM]^+[OTf]^-$, blue (◆) for $[BMIM]^+[BF_4]^-$, and green (◆) for $[BMIM]^+[Tf_2N]^-$, respectively.

4. Conclusions

This paper explored the feasibility of tailoring the gas transport properties of CA membranes by incorporating three distinct concentrations (10%, 20%, 30% wt.) of ILs, including $[BMIM]^+[BF_4]^-$, $[BMIM]^+[OTf]^-$, and $[BMIM]^+[Tf_2N]^-$. Various physicochemical characterization methods such as SEM, NMR, XRD, TGA, DSC, and tensile tests were employed to assess the fabricated MMMs. This revealed a complex effect of ILs that directly affect the transport through the affinity with the gas, and indirectly via changes in the crystallinity and polymer stiffness and co-plasticization by traces of residual humidity. The results confirmed that the addition of ILs, generally, shifted the CA's rigid semi-crystalline structure towards a more amorphous and rubber-like material, as evidenced by reductions in the glass transition temperature and Young's modulus. All in all, those contained $[BMIM]^+[Tf_2N]^-$ exhibited the lowest decline in crystallinity, and thermal and mechanical stability but reasonably kept the balance by enhancing CA's flexibility and elasticity of the CA. This can be attributed to the IL's more branched structure, lower molecular weight, and viscosity, which enhanced the effect of weak interactions with the CA polymeric matrix. Moreover, adding $[BMIM]^+[Tf_2N]^-$showed a stable and increasing trend in the transport properties of N_2, CO_2, and CH_4, compared to $[BMIM]^+[BF_4]^-$ and $[BMIM]^+[OTf]^-$, due to its consistent plasticizing effect without inducing CO_2 swelling. The decrease in Young's modulus and crystallinity causes a radical increase in diffusivity, with the strongest effect for the largest propane and

propene molecules thanks to the increased chain mobility which reduces the size-selectivity. While the Robeson plot confirmed a trade-off in CO_2/N_2 and CO_2/CH_4 separations, the separation performance for the C_3H_6/C_3H_8 pair was highly promising. The blended-membranes containing 30% $[BMIM]^+[Tf_2N]^-$ not only improved C_3H_6 permeability but also enhanced the selectivity of this pair compared to the neat CA membrane. This provides deeper insights into the continued development and application of the CA/IL blend membranes in the demanding propene/propane separation process. In summary, the precise effect of the IL on the transport properties of the CA/IL blend membranes is a complex combination of many different factors and this may lead to unclear trends at low IL content, while it creates a systematic increase in permeability and decrease in selectivity at higher concentrations of IL.

CRediT authorship contribution statement

Pegah Hajivand: Writing – original draft, Writing – review & editing, Investigation. **Mariagiulia Longo:** Writing – review & editing, Investigation. **Teresa Fina Mastropietro:** Writing – review & editing, Investigation. **Nicolas Godbert:** Writing – review & editing, Investigation. **Marcello Monteleone:** Writing – review & editing, Investigation. **C. Grazia Bezzu:** Writing – review & editing, Investigation. **Donatella Armentano:** Writing – review & editing, supervision, Funding acquisition. **Johannes C. Jansen:** Funding acquisition, Resources, Conceptualization, Writing – original draft, Writing – review & editing, Investigation, Supervision.

Acknowledgements

This research was partially funded by the European Union—NextGeneration EU from the Italian Ministry of Environment and Energy Security POR H2 AdP MMES/ENEA with involvement of CNR and RSE, PNRR—Mission 2, Component 2, Investment 3.5 “Ricerca e sviluppo sull’idrogeno”. CUP B93C22000630006

Declaration of competing interest

The authors declare no conflicts of interest.

Data statement

The data that support the findings of this study are available on request from the corresponding authors.

References

[1] R.L. Burns, W.J. Koros, Defining the challenges for C3H6/C3H8 separation using polymeric membranes, J Memb Sci 211 (2003) 299–309.

[2] D.S. Sholl, R.P. Lively, Seven chemical separations to change the world, Nature 532 (2016) 435–437.

[3] C. Staudt-Bickel, W.J. Koros, Olefin/paraffin gas separations with 6FDA-based polyimide membranes, J Memb Sci 170 (2000) 205–214.

[4] R.J. Swaidan, B. Ghanem, R. Swaidan, E. Litwiller, I. Pinnau, Pure-and mixed-gas propylene/propane permeation properties of spiro-and triptycene-based microporous polyimides, J Memb Sci 492 (2015) 116–122.

[5] K.-S. Liao, J.-Y. Lai, T.-S. Chung, Metal ion modified PIM-1 and its application for propylene/propane separation, J Memb Sci 515 (2016) 36–44.

[6] C. Zhang, K. Zhang, L. Xu, Y. Labreche, B. Kraftschik, W.J. Koros, Highly scalable ZIF-based mixed-matrix hollow fiber membranes for advanced hydrocarbon separations, AIChE Journal 60 (2014) 2625–2635.

[7] S. Park, M.R. Abdul Hamid, H.-K. Jeong, Highly propylene-selective mixed-matrix membranes by in situ metal–organic framework formation using a polymer-modification strategy, ACS Appl Mater Interfaces 11 (2019) 25949–25957.

[8] S. Fischer, K. Thümmler, B. Volkert, K. Hettrich, I. Schmidt, K. Fischer, Properties and applications of cellulose acetate, in: Macromol Symp, Wiley Online Library, 2008: pp. 89–96.

[9] E. Akbarzadeh, A. Shockravi, V. Vatanpour, High performance compatible thiazole-based polymeric blend cellulose acetate membrane as selective CO2 absorbent and molecular sieve, Carbohydr Polym 252 (2021) 117215.

[10] D. Nikolaeva, K. Verachtert, I. Azcune, J.C. Jansen, I.F.J. Vankelecom, Influence of ionic liquid-like cationic pendants composition in cellulose based polyelectrolytes on membrane-based CO2 separation, Carbohydr Polym 255 (2021) 117375.

[11] D.W. Wei, H. Wei, A.C. Gauthier, J. Song, Y. Jin, H. Xiao, Superhydrophobic modification of cellulose and cotton textiles: Methodologies and applications, Journal of Bioresources and Bioproducts 5 (2020) 1–15.

[12] X. Miao, J. Lin, F. Bian, Utilization of discarded crop straw to produce cellulose nanofibrils and their assemblies, Journal of Bioresources and Bioproducts 5 (2020) 26–36.

[13] A. Asad, D. Sameoto, M. Sadrzadeh, Overview of membrane technology, in: Nanocomposite Membranes for Water and Gas Separation, Elsevier, 2020: pp. 1–28.

[14] H. Li, S. Xu, B. Zhao, Y. Yu, Y. Liu, The phase structural evolution and gas separation performances of cellulose acetate/polyimide composite membrane from polymer to carbon stage, Membranes (Basel) 11 (2021) 618.

[15] V.K. Thakur, S.I. Voicu, Recent advances in cellulose and chitosan based membranes for water purification: A concise review, Carbohydr Polym 146 (2016) 148–165.

[16] M. Doosti, R. Abedini, Polyethyleneglycol-modified cellulose acetate membrane for efficient olefin/paraffin separation, Energy & Fuels 36 (2022) 10082–10095.

[17] B.Y. Gul, E. Pekgenc, V. Vatanpour, I. Koyuncu, A review of cellulose-based derivatives polymers in fabrication of gas separation membranes: Recent developments and challenges, Carbohydr Polym (2023) 121296.

[18] M. Guo, M. Kanezashi, Recent progress in a membrane-based technique for propylene/propane separation, Membranes (Basel) 11 (2021) 310.

[19] Z. Dai, R.D. Noble, D.L. Gin, X. Zhang, L. Deng, Combination of ionic liquids with membrane technology: A new approach for CO2 separation, J Memb Sci 497 (2016) 1–20.

[20] G. Kontos, C. Tsioptsias, I. Tsivintzelis, Cellulose Acetate–Ionic Liquid Blends as Potential Polymers for Efficient CO2 Separation Membranes, Polymers (Basel) 16 (2024) 554.

[21] B. Lam, M. Wei, L. Zhu, S. Luo, R. Guo, A. Morisato, P. Alexandridis, H. Lin, Cellulose triacetate doped with ionic liquids for membrane gas separation, Polymer (Guildf) 89 (2016) 1–11.

[22] A. Klemm, Y.-Y. Lee, H. Mao, B. Gurkan, Facilitated transport membranes with ionic liquids for CO2 separations, Front Chem 8 (2020) 637.

[23] A. Pinkert, K.N. Marsh, S. Pang, M.P. Staiger, Ionic liquids and their interaction with cellulose, Chem Rev 109 (2009) 6712–6728.

[24] A. Khakpay, P. Scovazzo, S. Nouranian, Homogeneous and biphasic cellulose acetate/room temperature ionic liquid membranes for gas separations: Solvent and phase-inversion casting vs. supported ionic liquid membranes, J Memb Sci 589 (2019) 117228.

[25] D. Nikolaeva, I. Azcune, M. Tanczyk, K. Warmuzinski, M. Jaschik, M. Sandru, P.I. Dahl, A. Genua, S. Lois, E. Sheridan, The performance of affordable and stable cellulose-based poly-ionic membranes in CO2/N2 and CO2/CH4 gas separation, J Memb Sci 564 (2018) 552–561.

[26] C.F. Martins, L. Neves, I.M. Coelhoso, F. Vaca Chavez, J.G. Crespo, P.J. Sebastião, Temperature Effects on the Molecular Dynamics of Modified Nafion® Membranes Incorporating Ionic Liquids' Cations: A 1H NMRD Study, Fuel Cells 13 (2013) 1166–1176.

[27] A.M. Lopez, M.G. Cowan, D.L. Gin, R.D. Noble, Phosphonium-based poly (ionic liquid)/ionic liquid ion gel membranes: influence of structure and ionic liquid loading on ion conductivity and light gas separation performance, J Chem Eng Data 63 (2018) 1154–1162.

[28] L.C. Tomé, A.S.L. Gouveia, C.S.R. Freire, D. Mecerreyes, I.M. Marrucho, Polymeric ionic liquid-based membranes: Influence of polycation variation on gas transport and CO2 selectivity properties, J Memb Sci 486 (2015) 40–48.

589 [29] D. Camper, J. Bara, C. Koval, R. Noble, Bulk-fluid solubility and membrane feasibility of Rmim-based
590 room-temperature ionic liquids, Ind Eng Chem Res 45 (2006) 6279–6283.

591 [30] M. Fallanza, M. González-Miquel, E. Ruiz, A. Ortiz, D. Gorri, J. Palomar, I. Ortiz, Screening of RTILs
592 for propane/propylene separation using COSMO-RS methodology, Chemical Engineering Journal 220
593 (2013) 284–293.

594 [31] V. Mokrushin, D. Assenbaum, N. Paape, D. Gerhard, L. Mokrushina, P. Wasserscheid, W. Arlt, H.
595 Kistenmacher, S. Neuendorf, V. Goeke, Ionic liquids for propene-propane separation, Chemical
596 Engineering & Technology: Industrial Chemistry-Plant Equipment-Process Engineering-
597 Biotechnology 33 (2010) 63–73.

598 [32] D. Camper, C. Becker, C. Koval, R. Noble, Low pressure hydrocarbon solubility in room temperature
599 ionic liquids containing imidazolium rings interpreted using regular solution theory, Ind Eng Chem Res
600 44 (2005) 1928–1933.

601 [33] S. Ramesh, R. Shanti, E. Morris, Employment of [Amim] Cl in the effort to upgrade the properties of
602 cellulose acetate based polymer electrolytes, Cellulose 20 (2013) 1377–1389.

603 [34] S. Ramesh, R. Shanti, E. Morris, Characterization of conducting cellulose acetate based polymer
604 electrolytes doped with “green” ionic mixture, Carbohydr Polym 91 (2013) 14–21.

605 [35] S. Ramesh, R. Shanti, E. Morris, Plasticizing effect of 1-allyl-3-methylimidazolium chloride in
606 cellulose acetate based polymer electrolytes, Carbohydr Polym 87 (2012) 2624–2629.

607 [36] S. Xu, H. Zhou, H. Jia, J. Xu, L. Ma, Y. Zang, P. Jiang, W. Ma, Y. Zhang, W. Zhao, Preparation and
608 high performance of cellulose acetate films by grafting with imidazole ionic liquid, ACS Omega 6
609 (2021) 12500–12506.

610 [37] D.Y. Xing, N. Peng, T.-S. Chung, Formation of cellulose acetate membranes via phase inversion using
611 ionic liquid,[BMIM] SCN, as the solvent, Ind Eng Chem Res 49 (2010) 8761–8769.

612 [38] H. Wang, G. Gurau, R.D. Rogers, Ionic liquid processing of cellulose, Chem Soc Rev 41 (2012) 1519–
613 1537.

614 [39] B. Lam, M. Wei, L. Zhu, S. Luo, R. Guo, A. Morisato, P. Alexandridis, H. Lin, Cellulose triacetate
615 doped with ionic liquids for membrane gas separation, Polymer (Guildf) 89 (2016) 1–11.

616 [40] A. Pinkert, K.N. Marsh, S. Pang, Reflections on the solubility of cellulose, Ind Eng Chem Res 49 (2010)
617 11121–11130.

618 [41] A. Brandt, J. Gräsvik, J.P. Hallett, T. Welton, Deconstruction of lignocellulosic biomass with ionic
619 liquids, Green Chemistry 15 (2013) 550–583.

620 [42] K.M. Gupta, Z. Hu, J. Jiang, Mechanistic understanding of interactions between cellulose and ionic
621 liquids: A molecular simulation study, Polymer (Guildf) 52 (2011) 5904–5911.

[43] R.C. Remsing, G. Hernandez, R.P. Swatloski, W.W. Massefski, R.D. Rogers, G. Moyna, Solvation of carbohydrates in N, N′-dialkylimidazolium ionic liquids: a multinuclear NMR spectroscopy study, J Phys Chem B 112 (2008) 11071–11078.

[44] J. Zhang, H. Zhang, J. Wu, J. Zhang, J. He, J. Xiang, NMR spectroscopic studies of cellobiose solvation in EmimAc aimed to understand the dissolution mechanism of cellulose in ionic liquids, Physical Chemistry Chemical Physics 12 (2010) 1941–1947.

[45] R.S. Payal, R. Bharath, G. Periyasamy, S. Balasubramanian, Density functional theory investigations on the structure and dissolution mechanisms for cellobiose and xylan in an ionic liquid: Gas phase and cluster calculations, J Phys Chem B 116 (2012) 833–840.

[46] T.G.A. Youngs, C. Hardacre, J.D. Holbrey, Glucose solvation by the ionic liquid 1, 3-dimethylimidazolium chloride: A simulation study, J Phys Chem B 111 (2007) 13765–13774.

[47] H. Liu, K.L. Sale, B.M. Holmes, B.A. Simmons, S. Singh, Understanding the interactions of cellulose with ionic liquids: a molecular dynamics study, J Phys Chem B 114 (2010) 4293–4301.

[48] B.D. Rabideau, A.E. Ismail, The effects of chloride binding on the behavior of cellulose-derived solutes in the ionic liquid 1-butyl-3-methylimidazolium chloride, J Phys Chem B 116 (2012) 9732–9743.

[49] T.G.A. Youngs, J.D. Holbrey, C.L. Mullan, S.E. Norman, M.C. Lagunas, C. D'Agostino, M.D. Mantle, L.F. Gladden, D.T. Bowron, C. Hardacre, Neutron diffraction, NMR and molecular dynamics study of glucose dissolved in the ionic liquid 1-ethyl-3-methylimidazolium acetate, Chem Sci 2 (2011) 1594–1605.

[50] B.D. Rabideau, A. Agarwal, A.E. Ismail, The role of the cation in the solvation of cellulose by imidazolium-based ionic liquids, J Phys Chem B 118 (2014) 1621–1629.

[51] A. Ito, S.-T. Hwang, Permeation of propane and propylene thrugh cellulosic polymer membranes, J Appl Polym Sci 38 (1989) 483–490. https://doi.org/10.1002/app.1989.070380308.

[52] M. Naghsh, M. Sadeghi, A. Moheb, M.P. Chenar, M. Mohagheghian, Separation of ethylene/ethane and propylene/propane by cellulose acetate–silica nanocomposite membranes, J Memb Sci 423 (2012) 97–106.

[53] W. Rattanawong, S. Osuwan, T. Rirksomboon, S. Kulprathipanja, The NaX-Zeolites/Cellulose acetate mixed matrix membrane for olefin/paraffin separation: Membrane technology in petrolum, petrochemical and gas processing, Preprints-American Chemical Society. Division of Petroleum Chemistry 46 (2001) 166–167.

[54] S. Sridhar, A.A. Khan, Simulation studies for the separation of propylene and propane by ethylcellulose membrane, J Memb Sci 159 (1999) 209–219. https://doi.org/10.1016/S0376-7388(99)00061-7.

[55] R.D. Rogers, K.R. Seddon, Ionic liquids--solvents of the future?, Science (1979) 302 (2003) 792–793.

[56] A. Bendaoud, Y. Chalamet, Effects of relative humidity and ionic liquids on the water content and glass transition of plasticized starch, Carbohydr Polym 97 (2013) 665–675.

[57] M. Murakami, Y. Kaneko, J. Kadokawa, Preparation of cellulose-polymerized ionic liquid composite by in-situ polymerization of polymerizable ionic liquid in cellulose-dissolving solution, Carbohydr Polym 69 (2007) 378–381.

[58] M. FitzPatrick, P. Champagne, M.F. Cunningham, The effect of subcritical carbon dioxide on the dissolution of cellulose in the ionic liquid 1-ethyl-3-methylimidazolium acetate, Cellulose 19 (2012) 37–44.

[59] D.Y. Xing, N. Peng, T.-S. Chung, Investigation of unique interactions between cellulose acetate and ionic liquid [EMIM] SCN, and their influences on hollow fiber ultrafiltration membranes, J Memb Sci 380 (2011) 87–97.

[60] S.C. Fraga, M. Monteleone, M. Lanč, E. Esposito, A. Fuoco, L. Giorno, K. Pilnáček, K. Friess, M. Carta, N.B. McKeown, A novel time lag method for the analysis of mixed gas diffusion in polymeric membranes by on-line mass spectrometry: Method development and validation, J Memb Sci 561 (2018) 39–58.

[61] H. Kono, H. Hashimoto, Y. Shimizu, NMR characterization of cellulose acetate: chemical shift assignments, substituent effects, and chemical shift additivity, Carbohydr Polym 118 (2015) 91–100.

[62] V.W. Goodlett, J.T. Dougherty, H.W. Patton, Characterization of cellulose acetates by nuclear magnetic resonance, J Polym Sci A1 9 (1971) 155–161.

[63] S. Nunes, F. Ramacciotti, A. Neves, E.M. Angelin, A.M. Ramos, É. Roldão, N. Wallaszkovits, A.A. Armijo, M.J. Melo, A diagnostic tool for assessing the conservation condition of cellulose nitrate and acetate in heritage collections: quantifying the degree of substitution by infrared spectroscopy, Herit Sci 8 (2020) 1–14.

[64] D. Larobina, L. Sanguigno, V. Venditto, G. Guerra, G. Mensitieri, Gas sorption and transport in syndiotactic polystyrene with nanoporous crystalline phase, Polymer (Guildf) 45 (2004) 429–436. https://doi.org/https://doi.org/10.1016/j.polymer.2003.11.009.

[65] Y. Tamai, Effective and efficient transport mechanism of CO2 in subnano-porous crystalline membrane of syndiotactic polystyrene, J Memb Sci 646 (2022) 120202. https://doi.org/https://doi.org/10.1016/j.memsci.2021.120202.

[66] V. Loianno, G. Guerra, B. Nagendra, G. Mensitieri, P. Musto, Unveiling the competitive diffusion of binary gas mixtures in polymers: The case of carbon dioxide and alkanes in nanoporous-crystalline polyphenylene oxide, Sep Purif Technol 341 (2024) 126953. https://doi.org/10.1016/j.seppur.2024.126953.

[67] L. Jiang, X. Huang, C. Tian, Y. Zhong, M. Yan, C. Miao, T. Wu, X. Zhou, Preparation and Characterization of Porous Cellulose Acetate Nanofiber Hydrogels, Gels 9 (2023) 484.

[68] A.C. Puleo, D.R. Paul, S.S. Kelley, The effect of degree of acetylation on gas sorption and transport behavior in cellulose acetate, J Memb Sci 47 (1989) 301–332.

[69] H.S. Barud, A.M. de Araújo Júnior, D.B. Santos, R.M.N. de Assunção, C.S. Meireles, D.A. Cerqueira, G. Rodrigues Filho, C.A. Ribeiro, Y. Messaddeq, S.J.L. Ribeiro, Thermal behavior of cellulose acetate produced from homogeneous acetylation of bacterial cellulose, Thermochim Acta 471 (2008) 61–69.

[70] X. Hou, J. Liu, H. Nguyen, H. Lin, Doping Polymers with Ionic Liquids to Manipulate Their Morphology and Membrane Gas Separation Properties, in: RSC Smart Materials, 2018: pp. 262–279.

[71] P. Yee, J.K. Shah, E.J. Maginn, State of hydrophobic and hydrophilic ionic liquids in aqueous solutions: are the ions fully dissociated?, J Phys Chem B 117 (2013) 12556–12566.

[72] M. Wohlert, T. Benselfelt, L. Wågberg, I. Furó, L.A. Berglund, J. Wohlert, Cellulose and the role of hydrogen bonds: not in charge of everything, Cellulose (2022) 1–23.

[73] R. Erdmann, S. Kabasci, H.-P. Heim, Thermal properties of plasticized cellulose acetate and its β-relaxation phenomenon, Polymers (Basel) 13 (2021) 1356.

[74] K. Friess, P. Izák, M. Kárászová, M. Pasichnyk, M. Lanč, D. Nikolaeva, P. Luis, J.C. Jansen, A Review on Ionic Liquid Gas Separation Membranes, Membranes (Basel) 11 (2021) 97. https://doi.org/10.3390/membranes11020097.

[75] K. Friess, J.C. Jansen, F. Bazzarelli, P. Izák, V. Jarmarová, M. Kačírková, J. Schauer, G. Clarizia, P. Bernardo, High ionic liquid content polymeric gel membranes: Correlation of membrane structure with gas and vapour transport properties, J Memb Sci 415 (2012) 801–809.

[76] M. Longo, M.P. De Santo, E. Esposito, A. Fuoco, M. Monteleone, L. Giorno, J.C. Jansen, Force spectroscopy determination of Young's modulus in mixed matrix membranes, Polymer (Guildf) 156 (2018) 22–29.

[77] P. Bernardo, J.C. Jansen, F. Bazzarelli, F. Tasselli, A. Fuoco, K. Friess, P. Izák, V. Jarmarová, M. Kačírková, G. Clarizia, Gas transport properties of Pebax®/room temperature ionic liquid gel membranes, Sep Purif Technol 97 (2012) 73–82.

[78] M. Klepić, A. Fuoco, M. Monteleone, E. Esposito, K. Friess, Z. Petrusová, P. Izák, J.C. Jansen, Tailoring the thermal and mechanical properties of PolyActiveTM poly (ether-ester) multiblock copolymers via blending with CO2-phylic ionic liquid, Polymers (Basel) 12 (2020) 890.

[79] A. Xu, J. Wang, H. Wang, Effects of anionic structure and lithium salts addition on the dissolution of cellulose in 1-butyl-3-methylimidazolium-based ionic liquid solvent systems, Green Chemistry 12 (2010) 268–275.

[80] M. Lalitha, S. Lakshmipathi, Interface energetics of [Emim]+[X]− and [Bmim]+[X]−(X= BF4, Cl, PF6, TfO, Tf2N) based ionic liquids on graphene, defective graphene, and graphyne surfaces, J Mol Liq 236 (2017) 124–134.

[81] L. Feng, Z. Chen, Research progress on dissolution and functional modification of cellulose in ionic liquids, J Mol Liq 142 (2008) 1–5.

[82] P.H. Daniels, A brief overview of theories of PVC plasticization and methods used to evaluate PVC-plasticizer interaction, Journal of Vinyl and Additive Technology 15 (2009) 219–223.

[83] E.H. Immergut, H.F. Mark, Principles of plasticization, in: ACS Publications, 1965.

[84] J.G. Wijmans, R.W. Baker, The solution-diffusion model: a review, J Memb Sci 107 (1995) 1–21.

[85] H. Wu, B. Kruczek, J. Thibault, A generalized model for the prediction of the permeability of mixed-matrix membranes using impermeable fillers of diverse geometry, J Memb Sci 641 (2022) 119951. https://doi.org/10.1016/J.MEMSCI.2021.119951.

[86] M.J. Muldoon, S.N.V.K. Aki, J.L. Anderson, J.K. Dixon, J.F. Brennecke, Improving carbon dioxide solubility in ionic liquids, Journal of Physical Chemistry B 111 (2007) 9001–9009. https://doi.org/10.1021/jp071897q.

[87] M. Kanakubo, T. Umecky, Y. Hiejima, T. Aizawa, H. Nanjo, Y. Kameda, Solution Structures of 1-Butyl-3-methylimidazolium Hexafluorophosphate Ionic Liquid Saturated with CO2: Experimental Evidence of Specific Anion−CO2 Interaction, J Phys Chem B 109 (2005) 13847–13850. https://doi.org/10.1021/jp052354o.

[88] S.N.V.K. Aki, B.R. Mellein, E.M. Saurer, J.F. Brennecke, High-pressure phase behavior of carbon dioxide with imidazolium-based ionic liquids, J Phys Chem B 108 (2004) 20355–20365.

[89] S.D. Hojniak, A.L. Khan, O. Holloczki, B. Kirchner, I.F.J. Vankelecom, W. Dehaen, K. Binnemans, Separation of carbon dioxide from nitrogen or methane by supported ionic liquid membranes (SILMs): influence of the cation charge of the ionic liquid, J Phys Chem B 117 (2013) 15131–15140.

[90] J. Deng, L. Bai, S. Zeng, X. Zhang, Y. Nie, L. Deng, S. Zhang, Ether-functionalized ionic liquid based composite membranes for carbon dioxide separation, RSC Adv 6 (2016) 45184–45192.

[91] Y. Wang, T.Y. Goh, P. Goodrich, M. Atilhan, M. Khraisheh, D. Rooney, J. Thompson, J. Jacquemin, Impact of ionic liquids on silver thermoplastic polyurethane composite membranes for propane/propylene separation, Arabian Journal of Chemistry 13 (2020) 404–415.

[92] M.-T. Vu, R. Lin, H. Diao, Z. Zhu, S.K. Bhatia, S. Smart, Effect of ionic liquids (ILs) on MOFs/polymer interfacial enhancement in mixed matrix membranes, J Memb Sci 587 (2019) 117157.

[93] S. Bai, S. Sridhar, A.A. Khan, Recovery of propylene from refinery off-gas using metal incorporated ethylcellulose membranes, J Memb Sci 174 (2000) 67–79.

[94] S.I. Semenova, Polymer membranes for hydrocarbon separation and removal, J Memb Sci 231 (2004) 189–207.

[95] V. Teplyakov, P. Meares, Correlation aspects of the selective gas permeabilities of polymeric materials and membranes, Gas Separation & Purification 4 (1990) 66–74.

[96] A. Fuoco, C. Rizzuto, E. Tocci, M. Monteleone, E. Esposito, P.M. Budd, M. Carta, B. Comesaña-Gándara, N.B. McKeown, J.C. Jansen, The origin of size-selective gas transport through polymers of intrinsic microporosity, J Mater Chem A Mater 7 (2019) 20121–20126.

[97] M.-L. Ge, R.-S. Zhao, Y.-F. Yi, Q. Zhang, L.-S. Wang, Densities and viscosities of 1-butyl-3-methylimidazolium trifluoromethanesulfonate+ H2O binary mixtures at T=(303.15 to 343.15) K, J Chem Eng Data 53 (2008) 2408–2411.

[98] J.E. Bara, T.K. Carlisle, C.J. Gabriel, D. Camper, A. Finotello, D.L. Gin, R.D. Noble, Guide to CO2 separations in imidazolium-based room-temperature ionic liquids, Ind Eng Chem Res 48 (2009) 2739–2751.

[99] R.L. Gardas, M.G. Freire, P.J. Carvalho, I.M. Marrucho, I.M.A. Fonseca, A.G.M. Ferreira, J.A.P. Coutinho, High-pressure densities and derived thermodynamic properties of imidazolium-based ionic liquids, J Chem Eng Data 52 (2007) 80–88.